

A Radiative Transfer Modeling Approach for Accurate Interpretation of PAM Fluorometry Experiments in Suspended Algal Cultures

Thomas E. Murphy

Exobiology Dept., NASA Ames Research Center, Moffett Field, CA 94035

Leslie E. Prufert-Bebout

Exobiology Dept., NASA Ames Research Center, Moffett Field, CA 94035

Brad M. Bebout

Exobiology Dept., NASA Ames Research Center, Moffett Field, CA 94035

DOI 10.1002/btpr.2394

Published online 00 Month 2016 in Wiley Online Library (wileyonlinelibrary.com)

The results of a numerical study on the simulation of pulse amplitude modulated (PAM) fluorometry within dense suspensions of photosynthetic microorganisms are presented. The Monte Carlo method was used to solve the radiative transfer equation in an algae-filled cuvette, taking into account absorption, anisotropic scattering, and fluorescence, as well as Fresnel reflections at interfaces. This method was used to simulate the transport of excitation and fluorescence light in a common laboratory fluorometer. In this fluorometer, detected fluorescence originates from a multitude of locations within the algal suspension, which can be exposed to very different fluence rates. The fluorescence-weighted fluence rate is reported, which is the local fluence rate of actinic light, averaged over all locations from which detected fluorescence originated. A methodology is reported for recovering the fluorescence-weighted fluence rate as a function of the transmittance of measuring light and actinic light through the sample, which are easily measured with common laboratory fluorometers. The fluorescence-weighted fluence rate can in turn be used as a correction factor for recovering intrinsic physiological parameters, such as the functional cross section of Photosystem II, from apparent (experimental) values. © 2016 American Institute of Chemical Engineers Biotechnol. Prog., 000:000–000, 2016

Keywords: PAM fluorometry, radiative transfer, photosynthesis, Photosystem II, algae, planktonic cultures, suspended cultures

Introduction

Pulse amplitude modulated (PAM) fluorometry is a powerful tool for quickly and noninvasively monitoring the physiological state of photosynthetic organisms.^{1–5} The general principle guiding fluorometric monitoring of photosynthesis is that chlorophyll fluorescence competes with photochemistry, enabling calculation of photosynthetic yield by measuring fluorescence yield.^{6–8} This method has gained wide popularity in photosynthesis research pertaining to leaves of vascular plants,^{5,9–11} macroalgae,¹² microbial mats,^{13,14} and suspended algal cultivation systems.^{15–23}

Background on PAM fluorometry

This section provides a brief outline of how PAM fluorometry is implemented experimentally to measure photosynthetic physiological parameters of microalgal cells. For greater detail, see, for example, Klughammer and Schreiber,²³ Murchie and Lawson,⁵ or Baker.⁴

A common application of PAM fluorometry is to measure a photosynthetic sample's rate of linear electron transport, or ETR, which is often regarded as a proxy for the total photosynthetic rate.^{23,24} The ETR can be written as²⁵

$$ETR = E \sigma_{II} Y_{II} \quad (1)$$

where the fluence rate, E , also known as the scalar irradiance, is the total photon flux at a point in space emanating from all directions, and has units of photons/m²s. The efficiency of Photosystem II, Y_{II} , is a unitless value between 0 and 1, and can be measured using a saturating pulse analysis.¹ Briefly, saturating pulse analysis entails measuring the fluorescence from cells in their normal state, and then again during exposure to a saturating light pulse which closes all electron transport chains within the sample. The difference in fluorescence signals between these two states is then used to calculate the photochemical yield.

The functional PSII cross section, σ_{II} , has units of m². Therefore, the scalar irradiance (units of photons/m²s) multiplied by the PSII cross section is the rate of cellular photon absorption (units of photons per second). The three parameters E , σ_{II} , and Y_{II} can all be wavelength dependent.

Correspondence concerning this article should be addressed to T. E. Murphy at thomasemurphy@utexas.edu.

A pump-and-probe technique can be used to measure the functional cross section of PSII, σ_{II} .^{23,26–28} In this technique, a measuring beam is applied to a culture at a frequency of about 10 kHz. The fluorescence signal resulting from the measuring beam is measured first with no actinic irradiance present, and then as an actinic pulse is switched on. Upon application of the actinic pulse, the fluorescence signal from the culture increases over a time scale of several milliseconds as a result of the closure of photosynthetic reaction centers. The exact relationship between the rate of fluorescence increase and the rate of reaction center closure can be determined using kinetic models of the electron transport chain reduction pathway, which are beyond the scope of this article (for details, see, for example, Laverne and Trissl²⁹). In a general sense, the rate of fluorescence increase is proportional to the rate of reaction center closure, k_{II} . In turn, the rate of reaction center closure is directly proportional to the rate of photon absorption by PSII²³

$$k_{II}(\lambda) = C\sigma_{II}(\lambda)E(\lambda) \quad (2)$$

where C is a constant, i.e., the number of photons required to close a reaction center, $\sigma_{II}(\lambda)$ is the functional PSII cross-sectional area and $E(\lambda)$ is the photon fluence rate in photons/m² s, each evaluated at wavelength λ .

Challenges for optically thick cultures

One inherent problem in fluorometric monitoring of planktonic (suspended) cultures is that the measured fluorescence emanates from a multitude of locations within the culture, and these locations can have very different local fluence rates. In the context of measuring the functional PSII cross section, σ_{II} , the temporal fluorescence rise upon application of an actinic pulse consists of contributions from cells exposed to a local fluence rate less than the intended fluence rate. This causes the rate of reaction center closure, and hence the rate of fluorescence rise, to be slower than it would be if all cells were exposed to the intended actinic fluence rate. This apparent reduction in the fluorescence rise rate, $\langle k_{II} \rangle$, causes the apparent (calculated) functional PSII cross section, $\langle \sigma_{II} \rangle$, to be less than the intrinsic functional PSII cross section, σ_{II} (Eq. 2).

One approach for minimizing the error caused by intra-sample light gradients is to perform fluorometric measurements on optically thin samples with small microorganism concentrations. However, decreasing the microorganism concentration also decreases the fluorescence signal to noise ratio, leading to greater measurement uncertainty. Additionally, diluting cells in water or fresh nutrient media can change their intrinsic photosynthetic properties, including, potentially, their functional PSII cross section. For these reasons, it is important to recover cells' actual (intrinsic) photosynthetic parameters from measured (apparent) fluorometric indices of dense cultures.

Klughhammer and Schreiber²³ presented a mathematical methodology for recovering the intrinsic PSII cross section from the apparent PSII cross section for dense cultures with appreciable light gradients.²³ First, they measured the fluorescence rise in very dilute suspensions and demonstrated that the rate constant of reaction center closure, k_{II} , increased linearly with the applied actinic fluence rate. Put differently, the *intrinsic* k_{II} increased linearly with the *local* E . Therefore, the relationship between the apparent (measured) $\langle k_{II} \rangle$ and the intrinsic $k_{II}(\lambda)$ can be written as

$$\frac{\langle k_{II}(\lambda) \rangle}{k_{II}(\lambda)} = \frac{\langle E(\lambda) \rangle}{E(\lambda)} \quad (3)$$

where $\langle E(\lambda) \rangle$ is the fluence rate averaged over all locations from which detected fluorescence originated, and $E(\lambda)$ is the incident fluence rate. The intrinsic PSII cross section can then be calculated using Eq. (2), using either the values $k_{II}(\lambda)$ and $E(\lambda)$, or the values $\langle k_{II}(\lambda) \rangle$ and $\langle E(\lambda) \rangle$. In either case, the values $E(\lambda)$ and $\langle E(\lambda) \rangle$, and therefore the spatial distribution of fluence rate within the cuvette, must be known.

Klughhammer and Schreiber also presented a straightforward methodology for calculating the fluence rate averaged over all detected fluorescence emission locations, $\langle E(\lambda) \rangle$. Generally, the methodology consists of calculating the spatial distribution of irradiance from both the measuring beam and actinic beam using the Beer-Lambert attenuation approximation. The spatial distributions of these two fluence rates are then used to calculate the actinic fluence rate averaged over all measuring beam absorption locations, $\langle E(\lambda) \rangle$. This method uses the assumption that fluorescence emanating from all regions of the sample reaches the detector with equal probability. However, the probability of a fluorescence quantum striking the detector is dependent on its location of emission due to (1) reabsorption of fluorescence quanta, (2) scattering of fluorescence quanta, and (3) variation in the view factor between the emission location and the detector. Moreover, the aforementioned model assumed one-dimensional (1-D) radiation transfer within the sample, wherein gradients in fluence rate exist only in the direction of beam propagation. However, light gradients also exist in both directions normal to beam propagation due to (1) divergence of a noncollimated beam and (2) Fresnel reflections and refractions at material interfaces. An accurate solution of the radiative transport model, which takes these effects into account, can enhance accuracy in calculating the fluorescence-averaged actinic irradiance, $\langle E(\lambda) \rangle$, and therefore the intrinsic PSII cross section, $\sigma_{II}(\lambda)$.

Radiative transport in algal environments

The metabolisms of an algal culture are highly sensitive to the light distribution within it, and a wide body of research addresses radiative transfer in algal cultures.³⁰ The existing models vary in complexity, from 1-D models, which are often sufficient to characterize light distributions within bioreactors with simple geometries,^{31–35} to 3-D models, which are necessary for multidirectional incident irradiance regimes and more complex bioreactor geometries.^{36–38} Calculation of light gradients within algal environments requires solution of the radiative transfer equation. In turn, the radiative transfer equation can be solved using a number of techniques, including the discrete ordinates method³⁹ and the Monte Carlo method.

Several studies have reported the use of Monte Carlo methods for modeling radiative transport in algal suspensions. Kirk⁴⁰ and Piskozub⁴¹ presented Monte Carlo solutions to the radiative transfer equation for use in ocean waters and algal suspensions. These solution methods were later used to analyze measurement errors in reflective absorption tubes⁴² and spectrophotometers.⁴³ Dauchet et al.⁴⁴ provide a descriptive overview of recent advances in Monte Carlo methods, specifically as they apply to radiative transfer in photobioreactors. However, to our knowledge, the 3-D

Monte Carlo method has not been applied to the problem of radiative transfer in PAM fluorometry experiments in algal suspensions.

There are two goals of the current study. The first goal is to present a 3-D radiative transport model of algal suspensions, and an associated Monte Carlo solution method to this model. The model explicitly takes into account absorption, anisotropic scattering, fluorescence, and Fresnel reflections and refractions at interfaces between gases, liquids, and solids. The second goal is to use the method to solve a problem pertaining to fluorometric analysis of dense algal suspensions. Specifically, radiative transfer is modeled within a Walz MULTI-COLOR-PAM, a versatile laboratory PAM fluorometer. The relationship is determined between the incident fluence rate, $E(\lambda)$, and the fluence rate averaged over all original locations of detected fluorescence, $\langle E(\lambda) \rangle$. The dependence of the ratio $\langle E(\lambda) \rangle / E(\lambda)$ on measuring wavelength, actinic wavelength, and microorganism density is investigated. The ratio $\langle E(\lambda) \rangle / E(\lambda)$ can be used as a correction factor for recovering the intrinsic PSII functional cross section from the apparent PSII cross section in optically thick cultures.

Analysis

Model description

The system under analysis is shown in Figure 1. The system geometry emulates the Walz MULTI-COLOR-PAM²² as closely as possible. This fluorometer was chosen as it is a versatile and commercially available PAM fluorometer with a wide variety of potential applications but is also subject to internal light gradients which can be elucidated by the present model. Measuring light and actinic light are both provided by an excitation light source, which is then transmitted via an excitation light guide toward a glass cuvette containing an algal suspension. A second light guide, the fluorescence emission light guide, is oriented at an angle of 90° with respect to the excitation light guide, and delivers fluorescence from the microorganisms to the detector.

The radiative transport equation serves as the model for photon transport within the algal suspension. The radiative transport equation can be written as^{39,45}

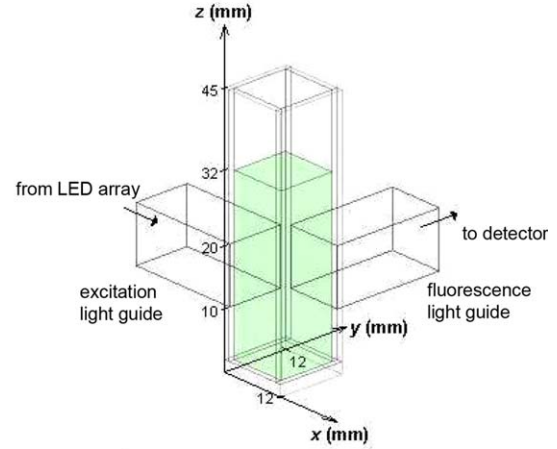
$$\frac{\partial I_\lambda(\hat{s})}{\partial \hat{s}} = -\kappa_\lambda I_\lambda(\hat{s}) - \sigma_\lambda I_\lambda(\hat{s}) + \frac{\sigma_\lambda}{4\pi} \int_{4\pi} I_\lambda(\hat{s}_i) \Phi_\lambda(\hat{s}_i, \hat{s}) d\Omega_i \quad (4)$$

where $I_\lambda(\hat{s})$ is the radiative intensity traveling in direction \hat{s} at wavelength λ , κ_λ is the absorption coefficient, σ_λ is the scattering coefficient, and Φ is the scattering phase function. The first and second terms on the right-hand side of Eq. (4) account for absorption and out-scattering from the direction of interest \hat{s} . The third term accounts for in-scattering of radiation traveling in all directions \hat{s}_i into the direction of interest \hat{s} .

Geometric optics serves as the model for photon transport at interfaces between air, glass, and water within the system. Specifically, the Fresnel relations are used to determine the refracted and reflected trajectories of rays upon intersecting a boundary between two different materials.

The primary quantity of interest in this study is the fluorescence-weighted fluence rate, $\langle E \rangle$. This quantity is defined as the fluence rate at the location of fluorescence

Perspective view



Top view

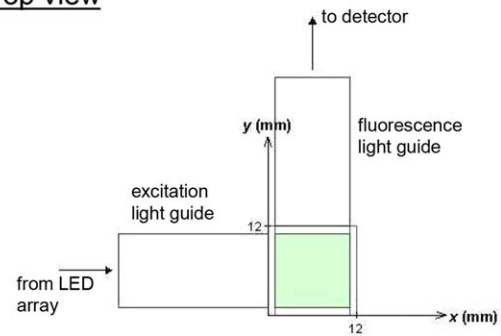


Figure 1. Geometry of the system under investigation, consisting of a cuvette containing an algal suspension, an excitation light guide providing measuring and actinic light, and a fluorescence light guide to carry fluorescence to the detector.

origin, averaged over all fluorescence photons that strike the detector, and can be written as

$$\langle E \rangle = \frac{1}{h} \sum_{h=1}^H E_h \quad (5)$$

where H is the total number of fluorescence photons that strike the detector, and E_h is the fluence rate of actinic light at the location of origin of fluorescence photon h . The fluorescence-weighted fluence rate is the effective fluence rate observed by the algal cells that contribute to the detected fluorescence signal. In this model, one fluorescence photon is emitted from every location at which a measuring photon is absorbed. In other words, no measuring beam photons are used for photochemistry or dissipated as heat.

Solution of the model

Overview of the Solution Method. The 3-D Monte Carlo method was used to solve both radiative transport in the algal suspension and Fresnel reflection and refraction at system boundaries. A description of the Monte Carlo ray tracing method is provided in, for example, Siegel and Howell⁴⁵ or Modest.³⁹ Briefly, the Monte Carlo method, first described by Metropolis and Ulam,⁴⁶ is a numerical method that uses random numbers to simulate physical systems in cases where analytical solutions are difficult or impossible. A Monte Carlo ray tracing method uses random numbers to track

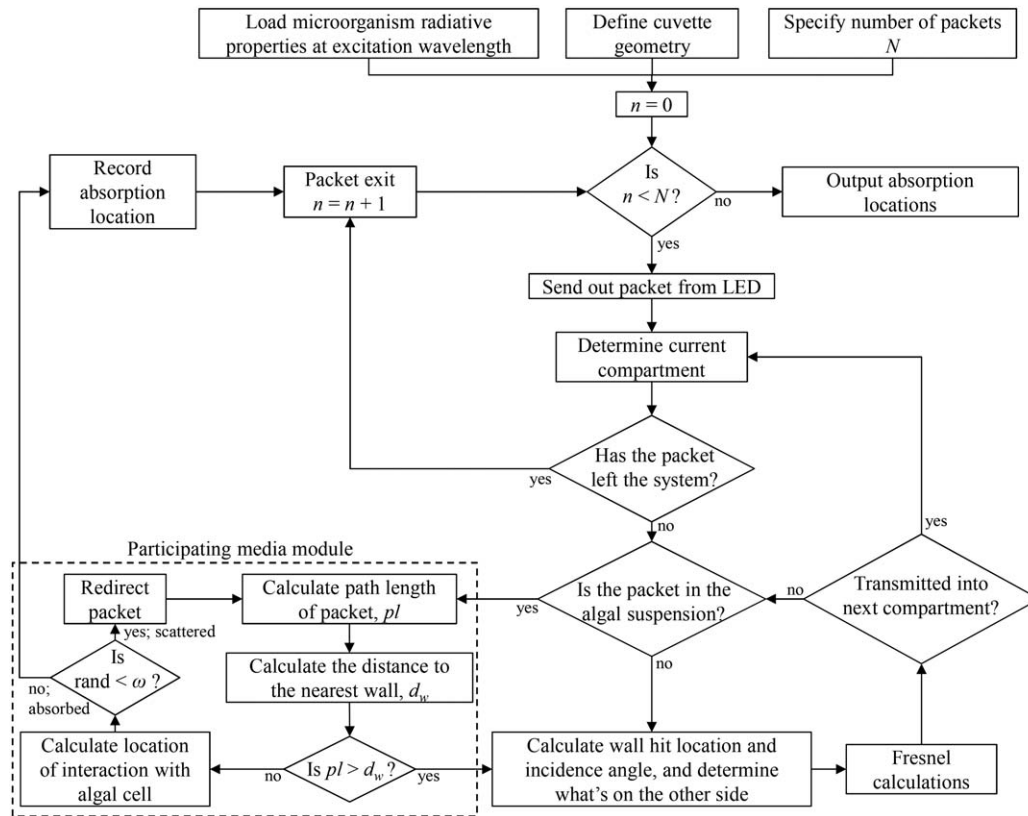


Figure 2. Flow chart of the excitation algorithm.

bundles, or packets, of photons through a system as they are scattered and absorbed by a participating medium. A multitude of resources describe recent advances in using the Monte Carlo method for transport problems such as the one in question here.^{44,47,48}

In the current study, it is of interest to simulate the spatial distribution of photon fluence rate (also known as the scalar irradiance) and fluorescence emission in a planktonic algal culture. To this end, the method presented here consists of two algorithms: the excitation algorithm and the fluorescence emission algorithm. In the excitation algorithm, packets of photons are incident onto one surface of a glass cuvette containing an algal culture. These packets are tracked until they are either absorbed by the algae or escape from the system. The spatial distribution of packet absorption is then used to calculate the spatial distribution of the photon fluence rate. The excitation algorithm is used to simulate the transport of both the measuring light and the actinic light.

The fluorescence emission algorithm accepts as input the absorption locations of measuring packets, and emits fluorescence packets from all of these locations. These fluorescence packets are tracked until they either strike the detector of the fluorometer or are lost from the system, either via absorption or escape. If an emission packet is detected, its location of origin is recorded, as well as the fluence rate at that location. The fluorescence-weighted fluence rate, $\langle E \rangle$, is calculated as the fluence rate at the location of fluorescence origin, averaged over all fluorescence packets that strike the detector.

Assumptions. In simulating radiative transport within the cuvette system, it is assumed that (1) the LED array is behind a diffuser, and the light emanating from the diffuser is perfectly diffuse (equal intensity in all forward directions),

(2) the light is randomly polarized, (3) the water and glass are nonabsorbing and nonscattering, as their absorption and scattering coefficients are negligible compared to that of the algae, and (4) fluorescence emission is randomly polarized, diffuse, and monochromatic at 687 nm, which is the wavelength of maximum chlorophyll fluorescence emission.⁴⁹ It is noted that chlorophyll fluorescence of microorganisms *in vivo* is not monochromatic, but rather has a half-width at half-maximum of about 15 nm. However, the spectral distribution of chlorophyll fluorescence is such that over half of the emitted photons are emitted at wavelengths between 682 and 692 nm.⁴⁹ Moreover, the absorption cross section of *Chlorella* sp. increases at wavelengths less than 687 nm and decreases at wavelengths greater than 687 nm, at approximately equal rates. For these reasons, considering monochromatic fluorescence at 687 nm is expected to provide similar results compared to considering the entire spectrum of chlorophyll fluorescence.

Excitation Algorithm. The purpose of the excitation algorithm is to track packets from the measuring and actinic beams through the cuvette and record their absorption locations. The spatial distribution of absorption locations from the actinic beam is then used to calculate the spatial distribution of actinic fluence rate. The excitation algorithm is summarized in Figure 2. Details on the numerical implementation of the excitation algorithm are given in Appendix A.

Calculation of Fluence Rate. The output of the excitation algorithm is a list of final packet locations, which can be inside the algae suspension if absorbed, or outside it if transmitted or reflected. The list of absorption locations is used to calculate the spatial distribution of fluence rate within the cuvette. For this, the cuvette is discretized in x , y , and z into rectangular volumes with dimensions δx , δy , and δz .

The values for δy and δz were each chosen to be 1 mm. The value for δx was chosen to correspond to an optical thickness of 0.002, based on the absorption coefficient. These values were selected to satisfy grid size independence, as the fluence rate distributions within the cuvette did not change significantly if the discretization sizes were doubled or halved. The photon absorption density in each discretized volume, A , is calculated as

$$A(x, y, z) = \frac{n_{abs}}{N_p} \frac{P_b}{X \delta x \delta y \delta z} \quad (6)$$

where n_{abs} is the number of packet absorption events in the discretized volume, N_p is the total number of packets sent out by the beam, P_b is the total power of the beam in photons/s, and X is the microorganism concentration in cells/mm³. Therefore, A has units of photons absorbed per cell per second. The fluence rate E is then calculated as

$$E(x, y, z) = \frac{A(x, y, z)}{A_{abs}} \quad (7)$$

where A_{abs} is the absorption cross section, in m²/cell.

Note that the above method for calculating fluence rate depends on the presence of microorganisms, as the photon absorption rate is used to calculate the fluence rate. However, it is useful to compare local fluence rates to a reference fluence rate. Here, the reference fluence rate is defined as the fluence rate at the center of the cuvette, at the center of the beam ($x = 6$ mm, $y = 6$ mm, $z = 15$ mm), with a microorganism concentration of zero. This location was chosen to be consistent with experimental setups.²³ To quantify this reference fluence rate, a simulated spherical fluence rate probe is placed at a location in the dead center of the cuvette, in the dead center of the beam. The microorganism concentration is set to zero, and packets are sent out from the LED array and tracked through the system. If a packet is in the liquid compartment, a check is performed to determine whether the packet hit the spherical sensor. To perform this check, the distance d from the packet at point \mathbf{p} and the sensor at point \mathbf{s} is calculated as⁵⁰

$$d = -(\mathbf{v} \cdot (\mathbf{p} - \mathbf{s})) \pm \sqrt{(\mathbf{v} \cdot (\mathbf{p} - \mathbf{s}))^2 - \|\mathbf{p} - \mathbf{s}\|^2 + r_s^2} \quad (8)$$

where \mathbf{v} is the packet direction and r_s is the sphere radius. If the discriminant on the right-hand side is non-negative, the packet hits the sphere, and a sensor hit is counted. The reference fluence rate is then calculated as

$$E_0 = \frac{(n_s/N_p)P_b}{A_{abs,p}} \quad (9)$$

where n_s is the number of packets that strike the spherical probe, N_p is the total number of packets, P_b is the beam power, and $A_{abs,p}$ is the absorption cross section of the probe, equal to πr^2 .

Calculation of Transmittance and Extinction. To calculate the transmittance of a sample, the fluorescence light guide is rotated by 90° such that it is opposite the excitation light guide. Moreover, the detector at the terminal end of the light guide is set to measure excitation packets, rather than fluorescence packets. The transmittance of a given sample was calculated as

$$\tau = T_{sample}/T_{blank} \quad (10)$$

where T_{sample} is the number of excitation packets that strike the detector, and T_{blank} is the number of packets that strike the detector for a microorganism concentration of zero. Finally, the extinction of the sample is calculated as

$$\epsilon = -\ln(\tau) \quad (11)$$

where \ln is the natural logarithm.

Fluorescence Emission Algorithm. The purpose of the fluorescence emission algorithm is to track fluorescence emission packets from measuring beam absorption locations. The algorithm then records the location of origin of all packets that strike the detector. The locations of detected fluorescence origin are then used, in conjunction with the spatial distribution of fluence rate, to calculate the fluorescence-weighted fluence rate, $\langle E \rangle$. The fluorescence emission algorithm is summarized in Figure 3. Details on the numerical implementation of the fluorescence emission algorithm are given in Appendix A.

The Fluorescence-Weighted Fluence Rate, $\langle E \rangle$. The fluorescence-weighted fluence rate, $\langle E \rangle$, is the output variable of primary interest in this study. It is defined as the actinic fluence rate averaged over all original locations of detected fluorescence

$$\langle E \rangle = \frac{1}{M} \sum_{m=1}^M E(x, y, z)_m \quad (12)$$

where M is the number of packets that hit the detector and $E(x, y, z)_m$ is the fluence rate at a packet's location of origin. The functional cross section of PSII, σ_{II} , can then be calculated as

$$\sigma_{II}(\lambda) = \langle k_{II}(\lambda) \rangle / \langle E(\lambda) \rangle \quad (13)$$

where $\langle k_{II}(\lambda) \rangle$ is the measured rate constant of reaction center closure, based on the rate of fluorescence rise upon application of the actinic pulse. This value is readily attainable using the MULTI-COLOR-PAM.

Validation of the Monte Carlo solution method

As the geometry in this system is quite specific, the participating media ray tracing algorithm (within the algae suspension) was validated separately from the Fresnel reflection and refraction algorithm. The participating media algorithm was validated by solving the I3RC⁵¹ “step cloud” problem, a 3-D radiative transfer problem with a known solution. The Fresnel reflection and refraction algorithm was validated by solving a multilayer radiative transfer problem for which an analytical solution is possible. For both algorithms, agreement with accepted solutions was within 1%. Further details of the validation methodology are provided in Appendix B.

Experiments simulated

In this study, a single simulated experiment consisted of (1) illuminating the cuvette with the measuring beam and recording absorption locations, (2) illuminating the cuvette with the actinic beam and calculating the fluence rate distribution $E(x, y, z)$, (3) emitting fluorescence from measuring beam absorption locations and recording the original locations of detected fluorescence, and (4) comparing these original locations against the matrix $E(x, y, z)$ to calculate the fluorescence-weighted fluence rate, $\langle E \rangle$. Input variables

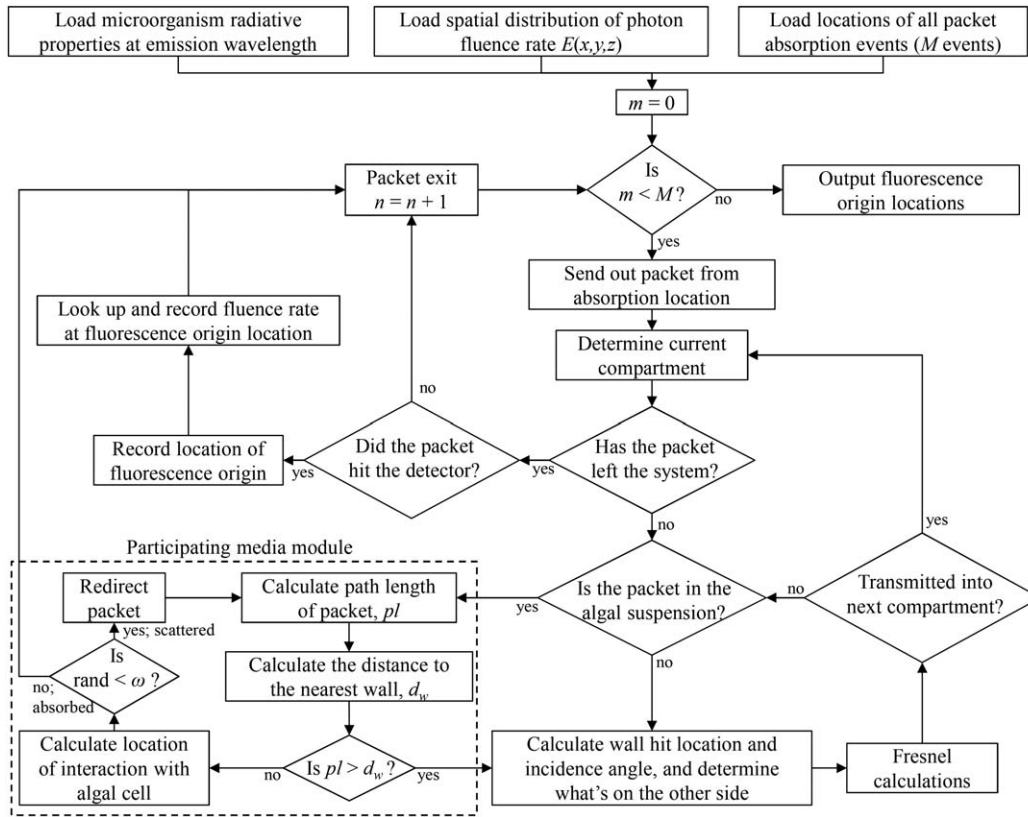


Figure 3. Flow chart of the fluorescence emission algorithm.

Table 1. Absorption (A_{abs}) and Scattering (S_{sca}) Cross Sections of *Chlorella* sp. at Peak Emission Wavelengths of LEDs in the MULTI-COLOR-PAM^{22*}

Wavelength (nm)	A_{abs} ($\text{m}^2/\text{cell} \times 10^{12}$)	S_{sca} ($\text{m}^2/\text{cell} \times 10^{12}$)
400	22.6	75.1
440	25.9	69.7
480	23.7	74.3
540	5.52	108
590	7.65	109
625	10.2	108
687	13.7	103

*Wavelengths given in nanometers (nm) and cross sections given in $\text{m}^2/\text{cell} \times 10^{12}$.⁵⁵

for each experiment were the measuring beam wavelength, actinic beam wavelength, and microorganism density. To be consistent with the MULTI-COLOR-PAM instrument, the measuring wavelengths investigated were 400, 440, 480, 540, 590, and 625 nm, and the actinic wavelengths investigated were 440, 480, 540, 590, and 625 nm. The investigated microorganism densities ranged from 10^5 to 10^8 cells/mL, which represents a typical experimental operating range. For all simulated experiments, the number of packets sent in the excitation algorithm, N_p , was 10^6 , which was selected to balance accuracy and computation time.

Microorganism Radiative Transport Parameters. As an exemplary microorganism, we used the green alga *Chlorella* sp. This organism is of interest in the biofuels market due to its high lipid productivity,⁵² as well as in the health food market due to its richness in protein, vitamins, polysaccharides, and polyunsaturated fatty acids.^{53,54} Moreover, its spectral absorption and scattering cross sections and scattering phase function were reported by Berberoglu et al.⁵⁵ Table 1

Table 2. Geometric Parameters of the System Under Analysis

Parameter	Size (mm)
Cuvette bottom thickness	2
Cuvette side thickness	1
Cuvette interior length (light path)	10
Cuvette interior height	43
Liquid height	30
Light pipe height from cuvette bottom	10
Light pipe width	10
Light pipe length	20
Gap distance*	0.001

*Between LED array and excitation light guide, excitation light guide and cuvette, cuvette and emission light guide, and emission light guide and detector.

gives absorption and scattering cross sections of *Chlorella* sp. at the wavelengths of peak emission of the measuring and actinic beams of the MULTI-COLOR-PAM, as well as at fluorescence emission wavelength. For all wavelengths, the Henyey-Greenstein average cosine, g , was 0.979.⁵⁵

Refractive Indices of Materials. The refractive indices of air, water, quartz, and acrylic are taken to be equal to 1.00, 1.33, 1.52, and 1.49, respectively.⁵⁶

Geometric Parameters. Table 2 provides a summary of the values used for each geometric parameter in the system, which is shown schematically in Figure 1.

Results and Discussion

Angular distribution of the incident irradiance

The angular distribution of the beam incident upon the cuvette is an important boundary condition which controls the light distribution within the cuvette. Most importantly,

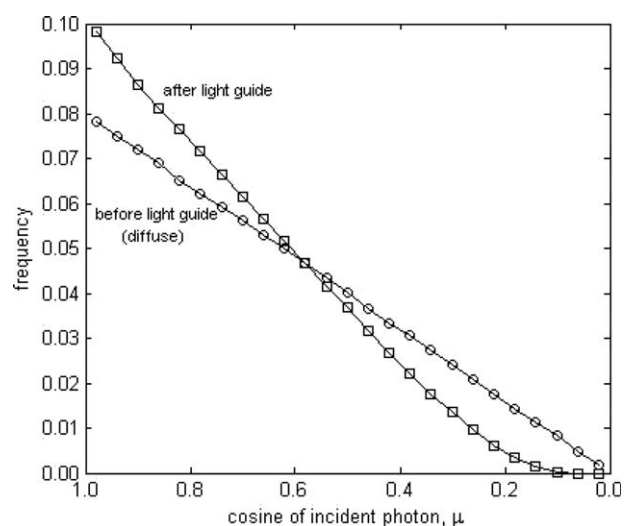


Figure 4. Angular distribution of diffuse irradiance, and of initially diffuse irradiance after passing through the acrylic light guide.

The parameter μ is the cosine of the angle between the packet trajectory and the surface normal of the cuvette.

the angular shape of the beam controls the rate of beam divergence within the cuvette, even in the absence of microorganisms.

The beam that eventually illuminates the cuvette begins as a diffuse beam emitted by an LED array behind a diffuser. This diffuse beam is emitted into air toward the acrylic excitation light guide. At the light guide, a fraction of the beam is reflected and the remainder is transmitted into the light guide. A fraction of the beam transmitted into the light guide exits the cuvette-facing side, while the remainder escapes out the sides of the light guide. Figure 4 shows the angular distribution of the irradiance from the diffuse LED array as well as the irradiance after passing through the acrylic light guide. The figure shows the frequencies of different cosines, μ , of the angle between the packet's trajectory and the surface normal of the cuvette. For diffuse irradiance, the frequency decreases linearly with decreasing μ because the projected area of the forward direction is directly proportional to μ . By comparison, the light guide serves to selectively transmit packets traveling in more forward directions due to (1) the lesser probability of transmission into the light guide for packets striking it at grazing angles and (2) escape of photons at grazing trajectories from the sides of the light guide. The mean cosines of the diffuse irradiance and the irradiance after passing through the light guide are 0.67 (exactly $2/3$ for diffuse emission) and 0.73, respectively. The light guide preserves the uniform spatial distribution of packets over the plane of the light guide. Therefore, the beam incident onto the cuvette consists of packets with uniform distribution over the square face of the light guide, with the angular distribution shown in Figure 4.

Fluence rate distribution in the cuvette

Figure 5 shows the spatial distribution of the actinic fluence rate at a wavelength of 590 nm within the cuvette for four different microorganism densities. This wavelength was selected to show trends as light absorption approached zero, as *Chlorella* sp. is weakly absorptive at this wavelength. In each panel, the local fluence rate is given as a fraction of the

reference fluence rate E_0 , the fluence rate at the center of the cuvette ($x = 6$ mm, $y = 6$ mm, $z = 15$ mm) for a microorganism concentration of zero. This case was chosen for the reference irradiance as it is straightforward to measure in an experimental setup using a scalar irradiance probe. The side view contour plots (top panel) represent the fluence rate at a y -value of 6 mm, representing the midplane of the cuvette. The top view contour plots (bottom panel) represent the fluence rate at a z -value of 15 mm, representing the midplane of the excitation light guide.

Figure 5a shows the fluence rate distribution for a microorganism concentration of 10^5 cells/mL. When the microorganism concentration was decreased below 10^5 cells/mL, the spatial distribution of fluence rate did not change significantly compared to the case of 10^5 cells/mL. Therefore, this fluence rate distribution can be considered the limiting distribution as the microorganism concentration approaches zero. It is important to note that significant spatial gradients of fluence rate were observed even in this limit of no microorganisms. In fact, in this limiting case, within the x - y plane at a z -value of 15 mm, the fluence rate varied from 59% to 113% of its value at the center of the cuvette. Variation was observed in both x and y dimensions due to (1) beam spreading and (2) the lesser probability of packets at grazing angles being transmitted into the liquid. Similar variation was observed in the x - z plane at a y -value of 6 mm. Averaged over the cubic volume bounded on the sides by the cuvette walls, and on the top and bottom by the top and bottom of the excitation light guide, the fluence rate in this limiting case was 67% of the reference fluence rate, E_0 . Note that this average fluence rate is different from the fluorescence-weighted fluence rate $\langle E \rangle$, which takes into account spatial nonuniformity in the measuring beam as well as the actinic beam.

Figure 5 also shows that as the microorganism concentration in the cuvette increased, fluence rate gradients became steeper due to absorption by the microorganisms. However, the general shape of the fluence rate distribution was conserved. The maximum fluence rate in all four cuvettes was about 1.1 times the reference fluence rate E_0 , and this maximum occurred at the location just inside the illuminated side of the cuvette, in the center of the beam. The fluence rate decreased with increasing distance from the center of the beam, as well as with increasing distance from the illuminated side. For the microorganism concentrations of 10^5 , 10^6 , 10^7 , and 10^8 cells/mL, the average fluence rate in the cubic volume bounded on the sides by the cuvette walls, and on the top and bottom by the top and bottom of the excitation light guide, was $0.67E_0$, $0.64E_0$, $0.45E_0$, and $0.08E_0$, respectively.

Effect of microorganism density on fluorescence-weighted fluence rate

For fluorometry applications, it is of interest to know the actinic fluence rate, averaged over all locations from which detected fluorescence originated, $\langle E \rangle$. This fluorescence-weighted fluence rate is dependent upon the spatial distributions of both actinic and measuring light. It is of interest in this section to quantify the fluorescence-weighted fluence rate, $\langle E \rangle$, as a function of the wavelengths of the actinic and measuring beams, as well as microorganism concentration. In this section $\langle E \rangle$ will be presented as a fraction of the reference fluence rate, E_0 , which can be readily

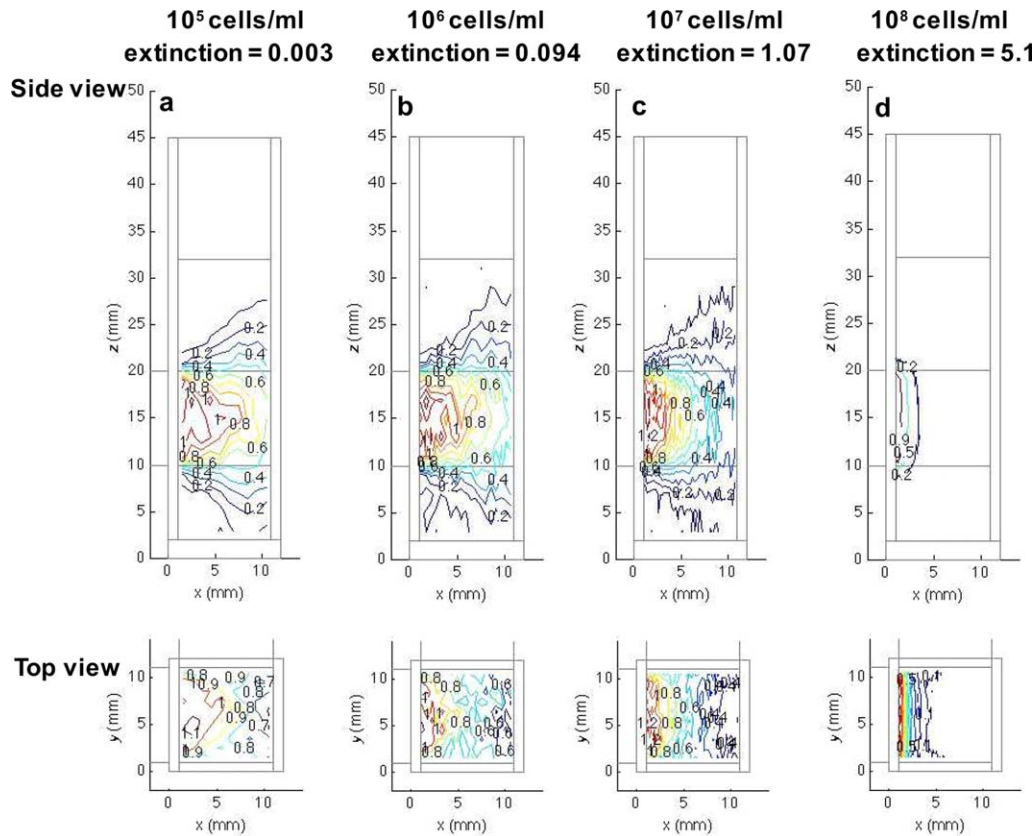


Figure 5. Spatial distribution of fluence rate at 590 nm in the cuvette at microorganism concentrations ranging from 10^5 cells/mL to 10^8 cells/mL.

Numbers on contour plots indicate the fluence rate as a fraction of the fluence rate at the center of the cuvette for the case of no microorganisms, E_0 .

measured. Moreover, the ratio $\langle E \rangle / E_0$ will be presented as a function of the measuring beam extinction and actinic beam extinction, as these parameters can be easier to measure than the microorganism concentration. Moreover, presenting $\langle E \rangle$ as a function of measuring and actinic extinction, rather than microorganism concentration, enables calculation of $\langle E \rangle$ for a wide range of algal strains, rather than solely for *Chlorella* sp.

Figure 6 shows, for four different microorganism concentrations, a top-down grayscale contour plot of the actinic fluence rate in the midplane of the beam ($z = 15$ mm), as well as the original emission locations of fluorescence quanta that struck the detector (marked in red). The actinic and measuring wavelengths were both 440 nm. For clarity, each panel shows only 10% of the original fluorescence locations with original z -locations between 14 and 16 mm. The white borders between the contour plots and the cuvette walls are an artifact of contour plotting function and the volume discretization. In all four cases, detected fluorescence emanated from a multitude of locations within the cuvette, each with a local actinic fluence rate not necessarily equal to the reference fluence rate E_0 . Therefore, in each case, the fluorescence-weighted fluence rate $\langle E \rangle$ was only a fraction of the reference fluence rate E_0 . Differences between $\langle E \rangle$ and E_0 were caused by (1) inhomogeneity in fluence rate from the actinic beam, (2) inhomogeneity in the absorption density of the measuring beam, and (3) inhomogeneity in the probability of fluorescence emanating from measuring beam absorption locations striking the detector. The magnitude of all three of these inhomogeneities increased with increasing

microorganism concentration, such that $\langle E \rangle$ decreased monotonically with increasing microorganism concentration for a given combination of measuring and actinic wavelengths.

The effect of spatially inhomogeneous probability of fluorescence striking the detector on $\langle E \rangle$ is clearly observed in Figure 6d: at the very high microorganism concentration of 10^8 cells/mL, the detected fluorescence predominantly originated from (1) the region of high measuring light absorption density near the excitation light guide and (2) the region near the fluorescence light guide, from which the probability of fluorescence reabsorption was low. Moreover, the region of greatest detected fluorescence density was in the corner near $(x, y) = (1 \text{ mm}, 10 \text{ mm})$, which satisfied both wall proximity criteria. Overall, for actinic and measuring wavelengths of 440 nm, the ratio of the fluorescence-weighted fluence rate to the reference fluence rate, $\langle E \rangle / E_0$, for microorganism concentrations of 10^5 , 10^6 , 10^7 , and 10^8 cells/mL were 0.70, 0.64, 0.42, and 0.38.

From an experimental perspective, it is useful to quickly ascertain the value of the ratio $\langle E \rangle / E_0$ based on the extinction of the measuring and actinic beams for a given sample. This ratio can be used as a correction factor to calculate, for example, the intrinsic wavelength dependent PSII cross section, σ_{II} . Figure 7 shows the ratio $\langle E \rangle / E_0$ for microorganism concentrations ranging from 10^5 to 10^8 cells/mL, measuring wavelengths of 400, 440, 480, 540, 580, and 625 nm, and actinic wavelengths of 440, 480, 540, 580, and 625 nm. These wavelengths were selected to be consistent with the Walz MULTI-COLOR-PAM instrument.

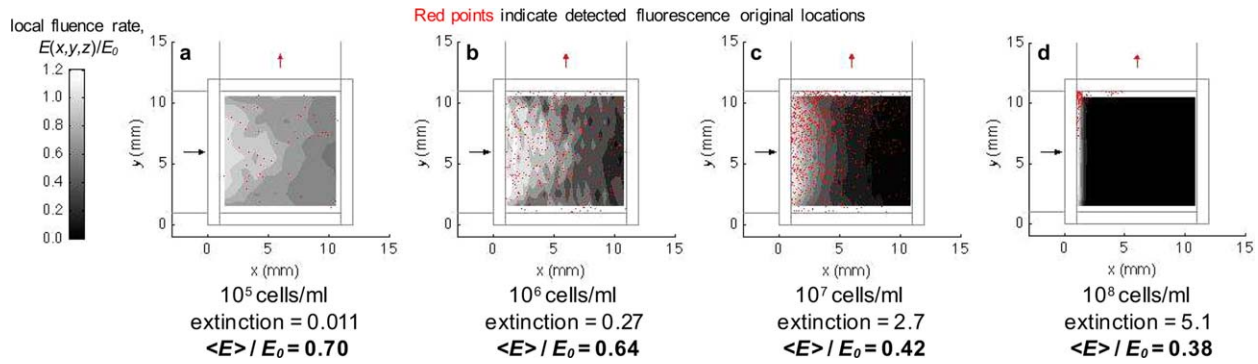


Figure 6. Local actinic fluence rate, normalized by E_0 (grayscale), and locations of detected fluorescence emission (red points) for microorganism concentrations ranging from 10^5 to 10^8 cells/mL.

The wavelength was 440 nm for both the actinic and measuring light. The plane height, z , was 15 mm, corresponding to the midplane of the light guides. The ratio $\langle E \rangle / E_0$ represents the ratio of fluorescence-weighted fluence rate to reference fluence rate.

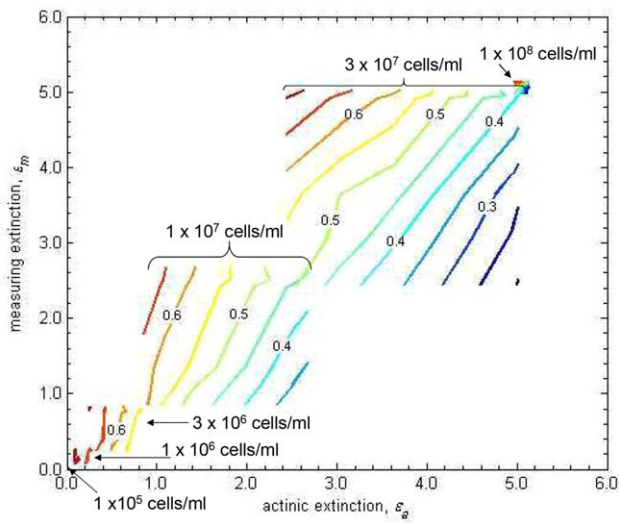


Figure 7. Ratio of the fluorescence-weighted fluence rate to the reference fluence rate, $\langle E \rangle / E_0$ (shown in color contours), as a function of the extinction values of measuring and actinic light.

In Figure 7, the numbers on the color contours show the value of the ratio $\langle E \rangle / E_0$, and each square cluster represents a different microorganism concentration. At all microorganism concentrations, the fluorescence-weighted fluence rate decreased with increasing extinction of actinic light, and increased with increasing extinction of measuring light, for the following reason. When the extinction of actinic light was small and the extinction of measuring light was large, the measuring light predominantly excited fluorescence at locations close to the excitation light guide, where the actinic fluence rate was high. On the other hand, when the extinction of actinic light was large and the extinction of measuring light was small, the measuring light penetrated deeper into the culture, where the actinic fluence rate was low, thereby decreasing the fluorescence-weighted fluence rate. For all microorganism concentrations, the value of the ratio $\langle E \rangle / E_0$ approached a maximum value of about 0.72 in the limit of small actinic extinction (540 nm) and large measuring extinction (440 nm). In the limit of large actinic extinction (440 nm) and small measuring extinction (540 nm), the ratio $\langle E \rangle / E_0$ approached a locally minimum value, which was inversely proportional to microorganism concentration. At the smallest tested microorganism

concentration of 10^5 cells/mL, this minimum value of $\langle E \rangle / E_0$ was not significantly different than its maximum value of 0.72. At the largest tested microorganism concentration of 10^8 cells/mL, this minimum value of $\langle E \rangle / E_0$ was 0.17.

Figure 7 serves as a guide for quickly obtaining the ratio $\langle E \rangle / E_0$ for a particular experiment. To do this, first an experimenter would measure the values of the extinction of measuring light and the actinic light through a sample in the MULTI-COLOR-PAM. Figure 7 is then used as a map, to locate the ratio $\langle E \rangle / E_0$ based on the actinic extinction (x -axis) and the measuring extinction (y -axis). For example, an experimental sample with an actinic extinction of 1.4 and a measuring extinction of 1.0 has an $\langle E \rangle / E_0$ value of 0.5. The fluorescence-weighted fluence rate $\langle E \rangle$ is then equal to 0.5 times the reference fluence rate E_0 , which readily measured as the fluence rate in the center of the same cuvette with no microorganisms. Using Eq. (13), the intrinsic cross section of Photosystem II, σ_{II} , is calculated by dividing the apparent rate constant of reaction center closure, $\langle k_{II} \rangle$ (output from the MULTI-COLOR-PAM), by $\langle E \rangle$.

Klughammer and Schreiber²³ also presented a methodology for calculating the ratio $\langle E \rangle / E_0$. The present model builds on the Klughhammer model by taking into account (1) 3-D, as opposed to 1-D, radiative transport, (2) spatial inhomogeneities in the probability of emitted fluorescence reaching the detector, and (3) Fresnel reflections at system boundaries. In the Klughhammer model, the ratio $\langle E \rangle / E_0$ was calculated as

$$\frac{\langle E \rangle}{E_0} = \frac{\epsilon_m}{\epsilon_m + \epsilon_a} \frac{1 - \tau_m \tau_a}{1 - \tau_m} \quad (14)$$

where ϵ and τ signify extinction and transmittance, respectively, and the subscripts a and m signify actinic and measuring light, respectively. Figure 8 compares the ratio $\langle E \rangle / E_0$ calculated using the Klughhammer model with the ratio $\langle E \rangle / E_0$ calculated in the present model, for all experiments simulated in the present study. In the limit as actinic and measuring extinctions approached zero, the value of $\langle E \rangle / E_0$ predicted by the Klughhammer model approached 1, whereas in the present study $\langle E \rangle / E_0$ approached 0.72. This discrepancy occurred because the Klughhammer model assumes a collimated beam, such that the fluence rate is uniform in the cuvette when no microorganisms are present. However, many fluorometers, including the MULTI-COLOR-PAM, have as a light source a beam that is much

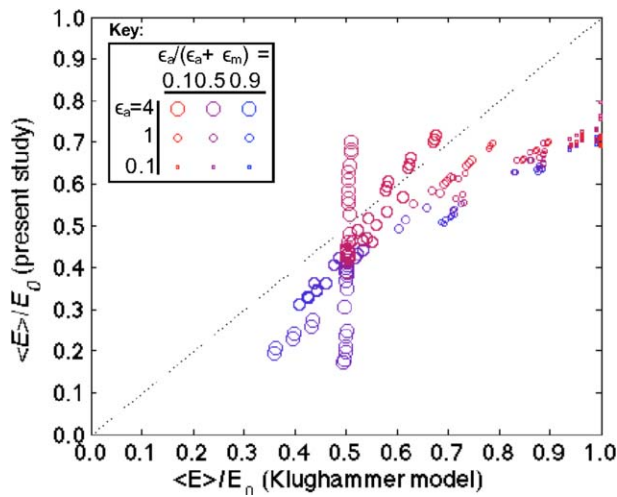


Figure 8. Comparison between fluence rate ratio $\langle E \rangle / E_0$ predicted by the model presented by Klughammer and Schreiber²³ and the ratio $\langle E \rangle / E_0$ predicted in the present study.

more accurately modeled as diffuse rather than collimated. The present model can take noncollimated angular beam shapes into account, whereas the Klughammer model cannot.

At greater extinctions, a clear trend between the ratio $\langle E \rangle / E_0$ determined in the current study and $\langle E \rangle / E_0$ calculated using the Klughammer model was not observed, though the $\langle E \rangle / E_0$ predicted by the current model was generally less than that predicted by the Klughammer model. Overall, the discrepancy between the two models, calculated as the absolute percent error, averaged over all simulated data points in Figure 8, was 33%.

One notable facet of the comparison between the two models is the nearly vertical line observed in Figure 8 at a $\langle E \rangle / E_0$ ratio (for the Klughammer model) of about 0.5. This line consists of data points with large actinic extinctions of about 4, and varying ratios of actinic extinction to measuring extinction. Near the top of the line, the actinic extinction is small compared to the measuring extinction, and vice versa near the bottom of the line. The steep nature of the line can be explained by the heterogeneity in the probability of fluorescence quanta reaching the detector, which is pronounced at high microorganism densities. As shown in Figure 6d, the measured fluorescence signal is dominated by fluorescence from two regions: the region near the excitation light source, and the region near the fluorescence detector. When the actinic extinction is large compared to the measuring extinction (bottom of the vertical line in Figure 8), fluorescence from the region near the detector significantly decreases the ratio $\langle E \rangle / E_0$, as that region generally has very low actinic irradiance. However, when the actinic extinction is small compared to the measuring extinction, the actinic irradiance is comparatively larger in the region near the detector, and as a result, fluorescence from this region does not decrease $\langle E \rangle / E_0$ as significantly. The variability in $\langle E \rangle / E_0$ for very similar values of the actinic extinction highlights the importance of considering the spatial heterogeneity in the probability of fluorescence quanta reaching the detector in calculating $\langle E \rangle / E_0$.

Conclusions

This article presented a 3-D radiative transport model for simulating PAM fluorometry in algal suspensions. The model

was solved using the Monte Carlo method. Spatial distributions of measuring light and actinic light were simulated within a cuvette illuminated by a common laboratory fluorometer (Walz, MULTI-COLOR-PAM). From the spatial distributions of measuring and actinic light, the fluorescence-weighted fluence rate was calculated, defined as the fluence rate of actinic light, averaged over all emission locations of fluorescence quanta that strike the fluorescence detector. This fluorescence-weighted fluence rate is essential for a wide range of fluorometry applications, including calculation of the intrinsic functional Photosystem II cross-sectional area of cells. The dependence of the fluorescence-weighted fluence rate on the wavelength of actinic and measuring light, as well as on microorganism concentration, was investigated. The reference actinic fluence rate was defined as the fluence rate in the dead center of the cuvette with a microorganism concentration of zero. It was observed that the fluorescence-weighted fluence rate decreased from 72% to 17% of the reference fluence rate as the microorganism concentration increased from 10^5 to 10^8 cells/mL (transmittances ranging from 0.991 to 0.006). Moreover, the difference between the fluorescence-weighted fluence rate and the reference fluence rate decreased as the ratio of measuring extinction to actinic extinction increased. A 2-D map was presented in which fluorescence-weighted fluence rate was given as a function of measuring and actinic extinctions. The map can be used to obtain “correction factors” to determine the intrinsic PSII cross section of algal cells in dense suspensions based on bulk measurements. Compared to previous studies that presented solutions radiative transfer approximations, the weighted fluence rates calculated in the current study varied by an average of about 33%. This study provides a first step for using 3-D Monte Carlo methods for simulating PAM fluorometry. In the future, this method can be improved by applying state of the art Monte Carlo techniques such as meshless calculation of fluence rate using backward sampling, and implementation for complex geometries.

Acknowledgments

The authors are grateful for the funding provided by the NASA Postdoctoral Program. The authors also sincerely thank Ulrich Schreiber for his helpful discussions. Finally, the authors are tremendously grateful to two anonymous reviewers, whose comments helped vastly improve the manuscript.

Notation

- A = photon absorption density, photons/cell s
- A_{abs} = absorption cross section, m^2/cell
- E = photon fluence rate (scalar irradiance), $\mu\text{mol photons}/m^2 \text{ s}$
- $\langle E \rangle$ = fluorescence-weighted fluence rate, $\mu\text{mol photons}/m^2 \text{ s}$
- F_m = maximum fluorescence signal during a saturating pulse
- F_o = baseline fluorescence signal
- N_p = number of packets sent out during a Monte Carlo simulation
- P_b = total power of a beam, $\mu\text{mol photons/s}$
- R = reflectance
- S_{sca} = scattering cross section, m^2/cell
- T = total number of transmitted packets
- X = microorganism concentration, cells/mL
- Y_{II} = photochemical yield of Photosystem II

a = first Euler rotation angle, rad
 b = second Euler rotation angle, rad
 d_w = distance to the nearest wall of a compartment, mm
 k_{II} = rate of electron transport chain closure, s^{-1}
 g = average scattering cosine in the Henyey-Greenstein phase function
 n = index of refraction
 n_{abs} = number of packet absorption events in a discretized volume
 \mathbf{p} = position vector
 pl = path length, mm
 r = random number between 0 and 1 with a uniform probability density function
 r_s = radius of fluence rate sensor, mm
 t = parametric time
 \mathbf{v} = parametric velocity vector
 $x = x$ coordinate in a Cartesian coordinate system
 $y = y$ coordinate in a Cartesian coordinate system
 $z = z$ coordinate in a Cartesian coordinate system

Greek symbols

β = extinction coefficient, mm^{-1}
 δ = discretization size, mm
 ε = extinction value of a sample
 θ = zenith angle, rad
 κ = absorption coefficient, mm^{-1}
 λ = wavelength, nm
 ρ = fraction of reflected energy at an interface
 Φ = scattering phase function
 ϕ = circumferential angle, rad
 σ = scattering coefficient, mm^{-1}
 σ_{II} = functional cross-sectional area of Photosystem II, nm^2
 τ = transmittance of a sample
 τ_x = optical thickness of a grid element
 ω = single scattering albedo

Subscripts

g = refers to global coordinate system
 i = refers to incident
 l = refers to trajectory within local coordinate system
 t = refers to transmitted
 w = refers to wall of a compartment

Abbreviations

ETR = electron transport rate
 PAM = pulse amplitude modulated
 PSII = Photosystem II

Literature Cited

- Genty B, Briantais J-M, Baker NR. The relationship between the quantum yield of photosynthetic electron transport and quenching of chlorophyll fluorescence. *Biochim Biophys Acta*. 1989;990:87–92.
- Schreiber U. Pulse-amplitude modulation (PAM) fluorometry and saturation pulse method: an overview. In: Papageorgiou GC, Govindjee, editors. *Chlorophyll a Fluorescence: A Signature of Photosynthesis*. Dordrecht, The Netherlands: Springer; 2004:279–319; ch. 11.
- Pfundel E. *JUNIOR-PAM Chlorophyll Fluorometer: Operator's Guide*. tech. rep. Effeltrich, Germany: Heinz Walz GmbH; 2007.
- Baker NR. Chlorophyll fluorescence: a probe to photosynthesis in vivo. *Ann Rev Plant Biol*. 2008;59:89–113.
- Murchie EH, Lawson T. Chlorophyll fluorescence analysis: a guide to good practice and understanding some new applications. *J Exp Bot*. 2013;64:3983–3998.
- Krause GH, Weis E. Chlorophyll fluorescence and photosynthesis: the basics. *Annu Rev Plant Physiol Plant Mol Biol*. 1991;42:313–349.
- Govindjee. Sixty-three years since Kautsky: chlorophyll a fluorescence. *Aust J Plant Physiol*. 1995;22:131–160.
- Maxwell K, Johnson GN. Chlorophyll fluorescence—a practical guide. *J Exp Bot*. 2000;51:659–668.
- Bilger W, Björkman O. Role of the xanthophyll cycle in photo-protection elucidated by measurements of light-induced absorbance changes, fluorescence and photosynthesis in leaves of *Hedera canariensis*. *Photosynth Res*. 1990;25:173–185.
- Demmig-Adams B, Adams WW III. Photoprotection and other responses of plants to high light stress. *Annu Rev Plant Physiol Plant Mol Biol*. 1992;43:599–626.
- Logan BA, Adams WW, Demmig-Adams B. Avoiding common pitfalls of chlorophyll fluorescence analysis under field conditions. *Funct Plant Biol*. 2007;34:853–859.
- Henley WJ, Levasseur G, Franklin LA, Osmond CB, Ramus J. Photoacclimation and photoinhibition in *Ulva rotundata* as influenced by nitrogen availability. *Planta*. 1991;184:235–243.
- Kühl M. Optical microsensors for analysis of microbial communities. *Method Enzymol*. 2005;397:166–199.
- Vopel K, Hawes I. Photosynthetic performance of benthic microbial mats in Lake Hoare, Antarctica. *Limnol Oceanogr*. 2006;51:1801–1812.
- Campbell D, Hurry V, Clarke AK, Gustafsson P, Öquist G. Chlorophyll fluorescence analysis of cyanobacterial photosynthesis and acclimation. *Microbiol Mol Biol R*. 1998;62:667–683.
- Flameling IA, Kromkamp J. Light dependence of quantum yields for PSII charge separation and oxygen evolution in eucaryotic algae. *Limnol Oceanogr*. 1998;43:284–297.
- Masojidek J, Grobbelaar JA, Pechar L, Koblizek M. Photosystem II electron transport rates and oxygen production in natural waterblooms of freshwater cyanobacteria during a diel cycle. *J Plankt Res*. 2001;23:57–66.
- Parkhill JP, Maillet G, Cullen JJ. Fluorescence-based maximal quantum yield for PSII as a diagnostic of nutrient stress. *J Phycol*. 2001;37:517–529.
- Kromkamp JC, Beardall J, Sukenik A, Kopecky J, Masojidek J, Bergeijk Sv, Gabai S, Shaham E, Yamshon A. Short-term variations in photosynthetic parameters of *Nannochloropsis* cultures grown in two types of outdoor mass cultivation systems. *Aquat Microb Ecol*. 2009;56:309–322.
- Sukenik A, Beardall J, Kromkamp JC, Kopecky J, Masojidek J, Bergeijk Sv, Gabai S, Shaham E, Yamshon A. Photosynthetic performance of outdoor *Nannochloropsis* mass cultures under a wide range of environmental conditions. *Aquat Microb Ecol*. 2009;56:297–308.
- Masojidek J, Vonshak A, Torzillo G. Chlorophyll fluorescence applications in microalgal mass cultures. In: *Chlorophyll a Fluorescence in Aquatic Sciences: Methods and Applications*. New York: Springer; 2010.
- Schreiber U, Klughammer C, Kolbowski J. *High-End Chlorophyll Fluorescence Analysis with the MULTI-COLOR-PAM. I. Various Light Qualities and Their Applications*. tech. rep. PAM Application Notes. Effeltrich, Germany: Heinz Walz GmbH; 2011.
- Klughammer C, Schreiber U. Apparent PS II absorption cross-section and estimation of mean PAR in optically thin and dense suspensions of *Chlorella*. *Photosynth Res*. 2015;123:77–92.
- Björkman O, Demmig B. Photon yield of O_2 evolution and chlorophyll fluorescence characteristics at 77 K among vascular plants of diverse origins. *Planta*. 1987;170:489–504.
- Ley AC, Mauzerall D. Absolute absorption cross sections for photosystem II and the minimum quantum requirement for photosynthesis in *Chlorella vulgaris*. *Biochim Biophys Acta*. 1982;680:95–106.
- Falkowski PG, Kolber Z. Variations in chlorophyll fluorescence yields in phytoplankton in the world oceans. *Aust J Plant Physiol*. 1995;22:341–355.
- Kolber ZS, Prásil O, Falkowski PG. Measurement of variable chlorophyll fluorescence using fast repetition rate techniques: defining methodology and experimental protocols. *Biochim Biophys Acta*. 1998;1367:88–106.
- Falkowski PG, Raven JA. *Aquatic Photosynthesis*, 2nd ed. Princeton, NJ, USA: Princeton University Press; 2007.
- Lavergne J, Trissl HW. Theory of fluorescence induction in photosystem II: derivation of analytical expressions in a model including exciton-radical pair equilibrium and restricted energy transfer between photosynthetic units. *Biophys J*. 1995;68:2474–2492.

30. Pilon L, Berberoğlu H, Kandilian R. Radiation transfer in photo-biological carbon dioxide fixation and fuel production by microalgae. *J Quant Spectrosc Ra*. 2011;112:2639–2660.
31. Suh IS, Lee SB. A light distribution model for an internally radiating photobioreactor. *Biotechnol Bioeng*. 2003;82:180–189.
32. Pottier L, Pruvost J, Deremetz J, Cornet JF, Legrand J, Dussap CG. A fully predictive model for one-dimensional light attenuation by *Chlamydomonas reinhardtii* in a torus photobioreactor. *Biotechnol Bioeng*. 2005;91:569–582.
33. Bosma R, Van Zessen E, Reith JH, Tramper J, Wijffels RH. Prediction of volumetric productivity of an outdoor photobioreactor. *Biotech Bioeng*. 2007;97:1108–1120.
34. Murphy T, Berberoğlu H. Effect of algae pigmentation on photobioreactor productivity and scale-up: a light transfer perspective. *J Quant Spectrosc Ra*. 2011;112:2826–2834.
35. Pruvost J, Cornet JF, Goetz V, Legrand J. Modeling dynamic functioning of rectangular photobioreactors in solar conditions. *AIChE J*. 2011;57:1947–1960.
36. Cornet J-F, Dussap C-G. A simple and reliable formula for assessment of maximum volumetric productivities in photobioreactors. *Biotechnol Prog*. 2009;25:424–435.
37. Wheaton ZC, Krishnamoorthy G. Modeling radiative transfer in photobioreactors for algal growth. *Comput Electron Agric*. 2012;87:64–73.
38. Kong B, Vigil RD. Simulation of photosynthetically active radiation distribution in algal photobioreactors using a multidimensional spectral radiation model. *Bioresour Technol*. 2014;158:141–148.
39. Modest MF. Radiative Heat Transfer. San Diego, CA: Academic Press; 2003.
40. Kirk JTO. Monte Carlo modeling of a reflective tube absorption meter. *Appl Opt*. 1992;31:6463–6468.
41. Piskozub J. Effects of surface waves and sea bottom on self-shading of in-water optical instruments. *Proc SPIE*. 1994;2258:300–308.
42. Piskozub J, Flatau PJ, Zaneveld JVR. Monte Carlo study of the scattering error of a quartz reflective absorption tube. *J Atmos Ocean Technol*. 2001;18:438–445.
43. Stramski D, Piskozub J. Estimation of scattering error in spectrophotometric measurements of light absorption by aquatic particles from three-dimensional radiative transfer simulations. *Appl Opt*. 2003;42:3634–3646.
44. Dauchet J, Blanco S, Cornet J-F, El Hafi M, Eymet V, Fournier R. The practice of recent radiative transfer Monte Carlo advances and its contribution to the field of microorganisms cultivation in photobioreactors. *J Quant Spectrosc Ra*. 2013;128:52–59.
45. Siegel R, Howell J. Thermal Radiation Heat Transfer, 4th ed. New York: Taylor & Francis; 2002.
46. Metropolis N, Ulam S. The Monte Carlo Method. *J Am Stat Assoc*. 1949;44:335–341.
47. Dimov IT. Monte Carlo Methods for Applied Scientists. Singapore: World Scientific Publishing Company; 2008.
48. Delatorre J, Baud G, Bezan JJ, Blanco S, Caliot C, Cornet JF, Coustet C, Dauchet J, El Hafi M, Eymet V, Fournier R, Gautrais J, Gourmel O, Joseph D, Meilhac N, Pajot A, Paulin M, Perez P, Piaud B, Roger M, Rolland J, Veynandt F, Weitz S. Monte Carlo advances and concentrated solar applications. *Sol Energy*. 2014;103:653–681.
49. Arnold W, Davidson JB. The identity of the fluorescent and delayed light emission spectra in *Chlorella*. *J Gen Physiol*. 1954;37:677–684.
50. Eberly DH. 3D Game Engine Design: A Practical Approach to Real-Time Computer Graphics, 2nd ed. Burlington, MA: Morgan Kaufmann; 2006.
51. Yetzer K, Varnai T, Huang S. *Intercomparison of 3D Radiation Codes*. Greenbelt, MD, USA: NASA Goddard Spaceflight Center; 2015. Available at <http://i3rc.gsfc.nasa.gov>. Accessed on February 12, 2016.
52. Chisti Y. Biodiesel from algae. *Biotechnol Adv*. 2007;25:294–306.
53. Pulz O, Gross W. Valuable products from biotechnology of microalgae. *Appl Microbiol Biot*. 2004;65:635–648.
54. Görs M, Schumann R, Hepperle D, Karsten U. Quality analysis of commercial *Chlorella* products used as dietary supplement in human nutrition. *J Appl Phycol*. 2009;22:265–276.
55. Berberoğlu H, Gomez PS, Pilon L. Radiation characteristics of *Botryococcus braunii*, *Chlorococcum littorale*, and *Chlorella* sp. used for CO₂ fixation and biofuel production. *J Quant Spectrosc Ra*. 2009;110:1879–1893.
56. Lide DR., editor. Handbook of Chemistry and Physics, 80th ed. Boca Raton, FL: CRC Press; 2000.
57. Karnopp DC, Margolis DL. Engineering Applications of Dynamics. Hoboken, NJ: Wiley; 2007.
58. Stark T. *Snell's Law in Vector Form*. Santa Barbara, CA, USA: Troy Stark; 2015. Available at <http://www.starkeffects.com/snells-law-vector.shtml>. Accessed on February 6, 2016.
59. Henyey G, Greenstein JL. Diffuse radiation in the galaxy. *Astrophys J*. 1941;93:70–83.

Appendix A: Ray Tracing Methodology for the Excitation and Fluorescence Emission Algorithms

This appendix provides detail on the numerical implementation of the Monte Carlo ray tracing method. For these calculations, the origin of the coordinate system is at the exterior bottom corner of the cuvette, shown in Figure 1. A particular ray is defined by its position $\mathbf{p} = [x, y, z]$, and its direction, $\mathbf{v} = [v_x, v_y, v_z]$, a unit vector. It is at times helpful to define the direction of a ray in spherical, rather than Cartesian coordinates. In this case, the ray's zenith angle, θ , is defined with respect to the z -axis, such that a ray traveling parallel to the z -axis and x -axis have θ values of 0 and $\pi/2$, respectively. The circumferential angle of a ray, ϕ , is defined with respect to the x -axis, such that a ray traveling parallel to the x -axis and y -axis have ϕ values of 0 and $\pi/2$, respectively.

Appendix A1: Excitation Algorithm

In the excitation algorithm, first a packet is sent out from the diffused LED array, which has a planar area equal to that of the light guide. The initial location of the packet is a random location, uniformly distributed across the face of the LED array. The emission direction is chosen from a Lambertian probability density function, which characterizes diffuse emission. To determine this direction, first, the coordinate system of the LED array is defined such that its z -axis points inward toward the cuvette (parallel to the global $+x$ -axis) and its x -axis points downward (parallel to the global $-z$ -axis). Within the coordinate system of the LED array, the initial packet direction (θ_l, ϕ_l) is selected as⁴⁵

$$[\theta_l, \phi_l] = [\sin^{-1}(r_\theta^{1/2}), 2\pi r_\phi] \quad (\text{A1})$$

where r_θ and r_ϕ are random numbers between 0 and 1 with a uniform probability density function. A coordinate transformation is performed to determine the packet's trajectory in the global coordinate system. For this, first the packet's trajectory within the local coordinate system (the coordinate system of the LED array) is converted to Cartesian parametric velocities

$$[v_x, v_y, v_z]_l = [\sin\theta_l \cos\phi_l, \sin\theta_l \sin\phi_l, \cos\theta_l] \quad (\text{A2})$$

Then, the Cartesian parametric coordinates within the local coordinate system $[v_x, v_y, v_z]_l$ are converted to Cartesian parametric coordinates within the global coordinate system $[v_x, v_y, v_z]_g$. This is done using the Euler angles⁵⁷

$$\begin{bmatrix} v_x \\ v_y \\ v_z \end{bmatrix}_g = \begin{bmatrix} \cos a & -\sin a \cos b & \sin a \sin b \\ \sin a & \cos a \cos b & -\cos a \sin b \\ 0 & \sin b & \cos b \end{bmatrix} \begin{bmatrix} v_x \\ v_y \\ v_z \end{bmatrix}_l \quad (\text{A3})$$

where a and b are the rotation angles that sweep the global coordinate system into the local coordinate system. For the case of the LED array, a and b are both equal to $\pi/2$. It is straightforward to calculate the packet's trajectory in the global coordinate system

$$[\theta, \phi]_g = [\cos^{-1}(v_{z,g}), \tan^{-1}(v_{y,g}/v_{x,g})] \quad (\text{A4})$$

The system under analysis is modeled as 13 interconnected compartments: two light guides, four air gaps on either end of each

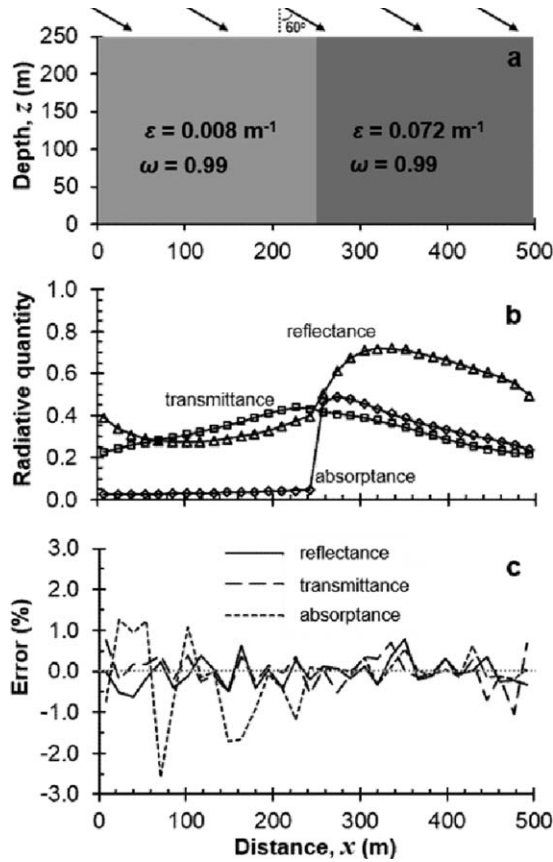


Figure A1. (a) Description of the I3RC step cloud problem used for model validation, (b) comparison of x -dependent transmittance, reflectance, and absorptance between the model used in the current study (symbols) and the I3RC consensus (lines), and (c) percent error between the results from the current model and the I3RC results.

light guide, four walls of the cuvette, the bottom of the cuvette, the liquid in the cuvette, and the air space above the liquid. After the global position and trajectory of a packet on the LED array is determined, that packet is inserted into the compartment consisting of the air gap between the LED array and the light guide. The packet is then allowed to travel between adjacent compartments until it either leaves the system at a boundary or is absorbed by the algae.

A compartment is described by the coordinates of its lower, left, front corner (i.e., the corner with the smallest x , y , and z coordinates), and its length in the x , y , and z directions. When a packet is in a particular compartment, the compartment's corner coordinates and size are used, along with the packet location and trajectory, to determine which compartment wall the packet will hit, the distance to the hit location, and the angle of incidence of the hit.

To calculate a packet's distance to the nearest wall, first, its compartment-centric coordinates are calculated as the packet's global position vector minus the compartment corner position vector. Then, the packet's trajectory is converted into Cartesian parametric coordinates according to Eq. (A2). Then, the parametric "time" required by the packet to strike the next wall in its path is calculated as

$$t_w = \min \left(\left[\frac{\Delta x_w}{v_x}, \frac{\Delta y_w}{v_y}, \frac{\Delta z_w}{v_z} \right] \right) \quad (\text{A5})$$

where Δx_w , Δy_w , and Δz_w are the distances to the walls normal to the x , y , and z directions, respectively, and v_x , v_y , and v_z are

the packet's parametric velocities in each direction. Equation (A5) states that the packet's trajectory will intersect three planes which contain three walls (top or bottom, left or right, and front or back), and the wall that the packet will actually hit corresponds to the minimum of the three times required to intersect each plane. The distance to that wall, d_w , is calculated as

$$d_w = |\mathbf{v}| t_w \quad (\text{A6})$$

where $|\mathbf{v}|$ is the magnitude of the velocity vector. The angle of incidence of the packet with respect to the unit normal to the wall, θ_i is calculated as

$$\theta_i = \cos^{-1}(\mathbf{v} \cdot \mathbf{n}) \quad (\text{A7})$$

where \mathbf{v} is the packet's trajectory and \mathbf{n} is the unit vector normal to the wall. The location at which the packet intersects the wall, \mathbf{p}_{hit} , is calculated as

$$\mathbf{p}_{hit} = \mathbf{p}_o + \mathbf{v} t_w \quad (\text{A8})$$

where \mathbf{p}_o is the packet's original position.

Upon striking a compartment wall, the hit location is used in conjunction with saved cuvette geometry information to determine which compartment is on the other side of the wall. The index of refraction of the next compartment is then determined. The packet reflectance at the interface is calculated using Fresnel's relations. Assuming unpolarized incident light, the reflectance, $\rho(\theta_i)$, is given by⁴⁵

$$\rho(\theta_i) = \frac{\sin^2(\theta_i - \theta_t)}{2\sin^2(\theta_i + \theta_t)} \left(1 + \frac{\cos^2(\theta_i + \theta_t)}{\cos^2(\theta_i - \theta_t)} \right) \quad (\text{A9})$$

where θ_i is the angle of incidence with respect to the wall surface normal, and θ_t is the transmitted angle, given by Snell's law as

$$n_t \sin \theta_t = n_i \sin \theta_i \quad (\text{A10})$$

where n_t and n_i are the indices of refraction on the transmitted and incident side of the interface. An exception to Eq. (A9) occurs if the incidence angle is exactly zero. In this case, the reflectance is equal to⁴⁵

$$\rho(\theta_i = 0) = \left(\frac{n_t - n_i}{n_t + n_i} \right)^2 \quad (\text{A11})$$

After the reflectance is calculated, a random number is selected between 0 and 1 with a uniform probability density function. If the number is less than the reflectance, the packet is reflected at the interface and remains in its current compartment. The reflected trajectory, \mathbf{v}_r , is calculated as⁵⁸

$$\mathbf{v}_r = \mathbf{v}_i - 2\mathbf{n}(\mathbf{v}_i \cdot \mathbf{n}) \quad (\text{A12})$$

where \mathbf{v}_i is the incident vector and \mathbf{n} is the wall unit normal vector. If the random number is greater than the reflectance, the packet is inserted into the next compartment with its transmitted trajectory. The transmitted trajectory is calculated as⁵⁸

$$\mathbf{v}_t = \frac{n_i}{n_t} [\mathbf{n} \times (-\mathbf{n} \times \mathbf{v}_i)] - \mathbf{n} \left(1 - \left(\frac{n_i}{n_t} \right)^2 |\mathbf{n} \times \mathbf{v}_i|^2 \right)^{1/2} \quad (\text{A13})$$

where \mathbf{v}_i is the incident trajectory, \mathbf{n} is the unit normal to the wall, and n_i and n_t are the indices of refraction on the incident and transmitted side of the interface.

The compartment containing the algae is the only participating medium in the system. If the packet is in this compartment, its path length prior to interaction with a particle, pl , is selected according to Beer's Law of exponential attenuation. In order to do this, the path length is selected as⁴⁵

$$pl = -\ln(r)/\beta(\lambda) \quad (\text{A14})$$

where \ln signifies the natural logarithm, r is a random number between 0 and 1 with uniform probability density, and $\beta(\lambda)$ is the extinction coefficient at wavelength λ , with units of mm^{-1} . The extinction coefficient is equal to the sum of the absorption coefficient $\kappa(\lambda)$ and the scattering coefficient $\sigma(\lambda)$

$$\beta(\lambda) = \kappa(\lambda) + \sigma(\lambda) \quad (\text{A15})$$

The absorption and scattering coefficients were calculated from their respective cross sections⁵⁵

$$[\kappa(\lambda), \sigma(\lambda)] = X[A_{\text{abs}}(\lambda), S_{\text{sca}}(\lambda)] \quad (\text{A16})$$

where $A_{\text{abs}}(\lambda)$ and $S_{\text{sca}}(\lambda)$ are the absorption and scattering cross sections, respectively, given in units of mm^2/cell , and X is the microorganism concentration in cells/mm^3 .

The distance from the packet's current location to the nearest wall along its trajectory is then computed (Eq. (A5)). If the distance to the wall is less than the path length, then the packet hits the wall, and Eqs. (A7–A11) are used to determine whether the packet is reflected or transmitted into the next compartment. If, on the other hand, the path length is less than the distance to the nearest wall, the packet strikes an algal cell. The location of this interaction, \mathbf{p}_{new} , is calculated as

$$\mathbf{p}_{\text{new}} = \mathbf{p}_{\text{old}} + pl\mathbf{v} \quad (\text{A17})$$

where \mathbf{p}_{old} and \mathbf{v} are the packet's old position and trajectory, respectively.

Upon striking a particle, a random number between 0 and 1 with uniform probability density is selected to determine whether the packet is scattered or absorbed. The single scattering albedo at wavelength λ , $\omega(\lambda)$, is defined as

$$\omega(\lambda) = \frac{\sigma(\lambda)}{\sigma(\lambda) + \kappa(\lambda)} \quad (\text{A18})$$

where $\sigma(\lambda)$ and $\kappa(\lambda)$ are the scattering and absorption coefficients, respectively. If the selected random number is less than the single scattering albedo, the packet is scattered. The scattered trajectory is then selected relative to the packet's current trajectory. The scattered zenith angle within this local coordinate system, θ_l , is selected using the scattering phase function of a single particle, which describes the probability of a ray being scattered into a particular angle with respect to its current trajectory.⁴⁵ In this study, the Henyey-Greenstein phase function is used, which has shown good agreement with the experimentally measured phase functions of many green algae, including *Chlorella* sp.⁵⁵ The Henyey-Greenstein phase function can be written as⁵⁹

$$\Phi(\theta_l) = \frac{1}{4\pi} \frac{1-g^2}{1+g^2-2g\cos\theta_l} \quad (\text{A19})$$

where Φ is the probability density function for the ray being scattered into the angle θ_l with respect to its current trajectory, and the parameter g is the average scattering cosine. To select a scattering angle using a random number, the cumulative integral of the Henyey-Greenstein phase function is computed, and the equation is rearranged for the scattered angle θ_l

$$\theta_l = \cos^{-1} \left(\frac{1}{2g} \left(1+g^2 - \left(\frac{1-g^2}{1+g(2r_\theta-1)} \right)^2 \right) \right) \quad (\text{A20})$$

where r_θ is a random number between 0 and 1 with uniform probability density. The scattered circumferential angle within the local coordinate system, ϕ_l , is selected as $2\pi r_\phi$, where r_ϕ is another random number between 0 and 1 with uniform

probability density. A coordinate transformation (Eqs. (A2–A4)) is then performed to place the scattered trajectory within the local coordinate system (θ_l, ϕ_l) back into the global coordinate system. In this case, the Euler angles a and b are equal to $\phi_{\text{old}} + \pi/2$ and θ_{old} , respectively.

If the random number associated with Eq. (A18) is greater than the single scattering albedo $\omega(\lambda)$, the packet is absorbed, and the absorption location is recorded. The packet tracking process is repeated for a specified number of packets N_p .

Appendix A2: Fluorescence Emission Algorithm

The emission algorithm accepts as input a complete list of the locations of the absorption events from the measuring beam, as well as the 3-D matrix of the fluence rate from the actinic beam, $E(x, y, z)$. For each absorption location, a fluorescence packet is emitted in a random direction, uniformly distributed over the entire sphere

$$[\theta, \phi] = [\cos^{-1}(2r_\theta-1), 2\pi r_\phi] \quad (\text{A21})$$

The fluorescence packet is then tracked through the cuvette using Eqs. (A14–A20), with the only difference being that the radiative properties are evaluated at the fluorescence emission wavelength. The packet is allowed to move through interconnected compartments until it is either reabsorbed, strikes the detector, or otherwise exits the system. If it strikes the detector, the original fluorescence location of the packet is recorded, as well as the actinic fluence rate at that location, using the matrix $E(x, y, z)$ as a lookup table.

Appendix B: Model Validation

As the geometry of the system under investigation was quite specific, different parts of the model were validated individually. Radiative transport modeling within the participating portion of the cuvette, i.e., the algae-containing compartment, was validated against established 3-D radiation transport codes. The compartment switching portion of the code was validated against simple cases for which analytical solutions exist. These two validation methods and results are described below.

Appendix B1: Participating Media Compartment Validation

The step cloud problem presented by NASA Goddard Spaceflight Center's Intercomparison of 3-D Radiation Codes (I3RC) info base⁵¹ was used to evaluate the accuracy of the 3-D Monte Carlo method developed in the present study. Although the step cloud problem does not include fluorescence, it is a truly 3-D problem which includes absorption and anisotropic scattering. Our solution to the step cloud problem was compared against the consensus results derived from the I3RC Phase I Workshop, which represent an accurate solution based on solutions by 17 independent codes written by researchers from several U.S. national laboratories and universities.

The step cloud problem is described in Figure A1a. The cloud consists of two equally sized partitions, each with a length, x , and a depth, z , of 250 m and infinite width, y , into the page. A periodic boundary condition exists such that the configuration shown in Figure A1a repeats infinitely in the positive and negative x -directions. Collimated radiation is uniformly incident onto the cloud at an angle of 60° with respect to normal to the cloud. The two compartments have extinction coefficients of 0.072 and 0.008 m^{-1} , and both compartments have a single scattering albedo ω of 0.99 and a Henyey-Greenstein average cosine g equal to 0.85.

The step cloud solution generated by the code written for the current study was compared to the I3RC solution on the basis of x -dependent reflectance, transmittance, and absorptance, as these

values were reported by the I3RC info base. Figure A1b shows the I3RC consensus results (lines) against the results from the model in the current study (symbols). For this validation case, the code for the current study tracked 10^7 packets. Agreement between the I3RC solution and the current model solution was very good. Figure A1c shows the percent error in x -dependent reflectance, transmittance, and absorptance, which indicates that none of these quantities were consistently over- or under-predicted by the model, and that there was no x -dependence of error magnitude. The magnitude of the discrepancy in absorptance (up to 2.6%) was larger than discrepancies in transmittance and reflectance because the absolute magnitude of absorptance in the optically thinner cloud was small, on average only about 0.033. Throughout the entire step cloud, the magnitudes of the errors in transmittance, reflectance, and absorptance were 0.32%, 0.28%, and 0.55%, respectively. This level of agreement was deemed acceptable for validating the participating media portion of the model.

Appendix B2: Compartment Switching Validation

To validate the compartment switching portion of the model, some simple cases were tested for which analytical solutions can be obtained. Namely, the reflectance and transmittance of a water-filled cuvette with no microorganisms were calculated for beam incidence angles of 0° and 20° . For incidence angles greater than 20° , analytical solutions became more difficult due to reflection and refraction from the cuvette sides. Following the ray tracing approach presented by Siegel and Howell,⁴⁵ the multilayer system consisting of, in the direction of ray propagation, air, glass, water, glass, and air, was modeled as two parallel glass windows, each having air on one side and water on the other. The reflectance of the entire system, R , is given by⁴⁵

$$R = R_1 + \frac{R_2 T_1^2}{1 - R_1 R_2} \quad (\text{B1})$$

where R_1 , R_2 , and T_1 are the reflectances of the first and second windows, and transmittance of the first window, respectively.

In the absence of absorption, the transmittance T_1 , is equal to $1 - R_1$. The reflectance of each window was determined using the ray tracing method presented by Siegel and Howell.⁴⁵ However, the method presented therein was modified to take into account the fact that the fraction of energy reflected at the water-facing side of each window was different than the fraction of energy reflected at the air-facing side. Taking this modification into account, the reflectances of the first and second windows, R_1 and R_2 , were calculated as

$$R_i = \rho_{i1} + \frac{(1 - \rho_{i1})(1 - \rho_{i1r})}{1 - \rho_{i1}\rho_{i2}} \quad (\text{B2})$$

where i is equal to 1 or 2 for the first or second window, ρ_{i1} is the fraction of reflected energy at the first interface in the forward direction, ρ_{i2} is the fraction of reflected energy at the second interface in the forward direction, and ρ_{i1r} is the fraction of reflected energy at the first interface in the backward direction. For the case of normal beam incidence, all three of these fractions are equal and calculated using Eq. (A11). For the case of non-normal incidence, the quantity ρ_{i1} was calculated using Eqs. (A9) and (A10). The angle of the transmitted ray with respect to the surface normal, θ_t , was then used in calculation of both ρ_{i2} and ρ_{i1r} , again using Eqs. (A9) and (A10).

The overall system reflectance, R , was calculated theoretically (Eqs. (B1) and (B2)), as well as using the numerical model with a number of packets N_p of 10^6 . The numerical model was run three times to quantify repeatability. For the case of normal beam incidence, the total reflectances calculated theoretically, and using the model (\pm standard deviation) were 0.08915 and 0.08909 ± 0.00010 . For the case of 20° incidence, the theoretical and model-calculated reflectances were 0.08967 and 0.08970 ± 0.00015 . This level of agreement was deemed acceptable for validating the compartment switching algorithm.

Manuscript received Mar. 24, 2016, and revision received Oct. 26, 2016.